J. Fluid Mech. (2000), *vol.* 407, *pp.* 57–84. Printed in the United Kingdom

Turbulent thermal convection in a cell with ordered rough boundaries

By Y.-B. DU AND P. TONG†

Department of Physics, Oklahoma State University, Stillwater, OK 74078, USA

(Received 23 December 1998 and in revised form 9 November 1999)

A novel convection experiment is conducted in a cell with rough upper and lower surfaces. The measured heat transport in the rough cell is found to be increased by more than 76%. Flow visualization and near-wall temperature measurements reveal new dynamics for the emission of thermal plumes. The experiment shows that the interaction between the horizontal shear flow due to the large-scale circulation and the ordered rough surface creates a secondary flow (eddies) in the groove region. The secondary flow together with the large-scale circulation enhance the detachment of the thermal boundary layer from the tip of the rough elements. These extra thermal plumes are responsible for the enhanced heat transport in the rough cell. The discovery of the enhanced heat transport has important applications in engineering for more efficient heat transfer.

1. Introduction

The discovery of scaling laws in the heat transport and temperature statistics in turbulent Rayleigh–Bénard convection (Heslot, Castaing & Libchaber 1987; Castaing *et al.* 1989; Wu *et al.* 1990) has stimulated many experimental (Solomon & Gollub 1990, 1991; Tong & Shen 1992; Chillá *et al.* 1993; Belmonte, Tilgner & Libchaber 1993, 1995*a*; Shen, Xia & Tong 1995; Takeshita *et al.* 1996; Xin, Xia & Tong 1996; Cioni, Ciliberto & Sommeria 1997; Chavanne *et al.* 1997), numerical (Deluca *et al.* 1990; Werne 1993, 1994; Kerr 1996), and theoretical (Castaing *et al.* 1989; She 1989; Shraiman & Siggia 1990; Siggia 1994; Grossmann & Lohse 2000) efforts, aimed at explaining, testing, and finding new scaling laws in the temperature and velocity fields. The experiment carried out by the Chicago group (Heslot *et al.* 1987; Castaing *et al.* 1989) confirmed that the normalized heat flux, or the Nusselt number Nu, scales with the Rayleigh number as $Nu \sim Ra^{2/7}$, which is different from the classical $Ra^{1/3}$ scaling (Kraichnan 1962). Like many transport phenomena in condensed matter physics, the measured macroscopic transport properties can often be explained by theories with different microscopic mechanisms. Several theoretical models (Castaing *et al.* 1989; She 1989; Shraiman & Siggia 1990; Siggia 1994; Grossmann & Lohse 2000) have been proposed recently to explain the measured $Ra^{2/7}$ scaling in turbulent heat transport. The theoretical calculations arrive at similar conclusions for the temperature field, but have different assumptions and predictions for the velocity field in the turbulent bulk region and near the thermal and viscous boundary layers. There are two salient features in turbulent convection, which are related directly to the transport of heat across the convection cell. One is the large-scale circulation that spans the height of

† To whom correspondence should be addressed. E-mail: ptong@osuunx.ucc.okstate.edu.

the cell, and the other is intermittent bursts of thermal plumes from the upper and lower thermal boundary layers. A main issue of an unresolved theoretical debate is whether the heat transport in turbulent convection is determined primarily by the thermal plumes or by the large-scale circulation (Siggia 1994).

To find the real mechanism for the turbulent heat transport, it becomes important to alter the boundary conditions of the cell and determine the relative contributions of the thermal plumes and the large-scale circulation to the total heat transport. Recent experiments have shown that the $Ra^{2/7}$ scaling is a robust and general feature of turbulent convection and remains unchanged under various perturbations, such as horizontal shearing of a boundary layer (Solomon & Gollub 1990, 1991), vertical rotation of the whole convection cell (Liu & Ecke 1997), change of convecting fluids with different Prandtl numbers (Takeshita *et al.* 1996; Cioni, Ciliberto & Sommeria 1996, 1997), and alteration of the large-scale circulation by introducing bluff obstacles on the conducting plates (Ciliberto, Cioni & Laroche 1996) and sidewalls (Xia & Lui 1997). The $Ra^{2/7}$ scaling was also observed in a convection cell heated from the side (Belmonte, Tilgner & Libchaber 1995*b*). These experiments indicate that the heat transport in turbulent convection is controlled by the local dynamics near the thermal boundary layers and the current theories seem to be too restrictive in explaining the observed scaling laws.

In this paper, we report a new convection experiment carried out in a cell with rough upper and lower surfaces. The measured heat transport in the rough cell is found to be increased by more than 76%. Flow visualization and near-wall temperature measurements reveal new dynamics for the emission of the thermal plumes. The experiment shows that the interaction between the horizontal shear flow (due to the large-scale circulation) and the ordered rough surface creates a secondary flow (eddies) in the groove region. This secondary flow together with the large-scale circulation enhance the detachment of the thermal boundary layer from the tip of the rough elements. The extra thermal plumes detached from the rough surfaces are responsible for the enhanced heat transport. The striking effect of the surface roughness provides new insights into the roles played by the thermal plumes in determining the heat transport in turbulent convection. The discovery of the enhanced heat transport in the rough cell has important applications in engineering, geography, and meteorology. An example is convection in the atmosphere and oceans, where the underlying surfaces are almost always rough. Understanding heat transport phenomena in thermal convection will shed new light on technological improvements for more efficient heat transfer in various industrial applications ranging from heat exchangers to a re-entry vehicle.

Our current knowledge about the roughness effect on turbulent flows comes largely from experiments in wind tunnels and other open systems (Raupach, Antonia & Rajagopalan 1991), in which the disturbance flow produced by a rough wall is confined in the near-wall region and is quickly discharged downstream. Because of these reasons the surface roughness usually does not perturb the turbulent bulk region very much, and its effect is often described by rescaling the relevant parameters with the surface roughness height h (Tennekes & Lumley 1972). This situation is changed completely for flows in a closed cell, in which the disturbances produced by the boundary are inevitably mixed into the turbulent bulk region. In recent years, much attention has been focused on the basic structures of turbulent eddies near a wall and their influence on turbulent drag (Choi, Moin & Kim 1993; Moin & Bewley 1994; Moin & Kim 1997). Longitudinal grooves (also called riblets) and other surface structures are introduced to reduce the drag caused by turbulence (Riley, Gad-el-Hak & Metcalfe 1988; Walsh 1990; Choi *et al.* 1993). Experimental studies of

turbulent transport are difficult because of the severe requirements on spatial and temporal resolutions in visualizing a rapidly evolving velocity field and on accuracy in simultaneous measurements of the local velocity and turbulent drag. Turbulent thermal convection, on the other hand, is a unique and ideal system for the study of the boundary layer dynamics. Temperature as a scalar field can be measured and visualized readily with high spatial and temporal resolutions. Moreover, the local temperature measurement and flow visualization can be performed simultaneously, together with an accurate determination of the heat transport across the cell. Our recent studies of turbulent thermal convection in both the smooth and rough cells (Shen, Tong & Xia 1996; Du & Tong 1998) have shown that a comparative study of turbulent transport under different boundary conditions can greatly benefit our understanding of the structure and dynamics of the turbulent boundary layers. In this paper, we present a systematic study of the boundary layer dynamics near an ordered rough surface in turbulent convection. Some of the results have been reported previously in a rapid communication (Du & Tong 1998).

The remainder of the paper is organized as follows. We first describe apparatus and experimental methods in § 2. Experimental results are discussed in § 3. Finally, the work is summarized in § 4.

2. Apparatus and experimental methods

2.1. *Convection cells*

The experiment is conducted in a vertical cylindrical cell filled with water. Figure 1(*a*) shows a sketch of the smooth and rough cells used in the experiment. The sidewall of the cells is made of transparent Plexiglas with an inner diameter of 20 cm. Two Plexiglas rings with the same diameter but having two different heights of 20 cm and 40 cm are used, respectively, to extend the accessible range of the Rayleigh number. The corresponding aspect ratios (A = diameter/height) are 1.0 and 0.5. The top and bottom plates of the cells are made of brass and their surfaces are electroplated with a thin layer of gold. Two silicone rubber film heaters (Omega, SRFR 7/10) are connected in parallel and sandwiched on the backside of the bottom plate to provide a constant and uniform heating. A DC power supply with a 0.1% long-term stability is used to provide the heating power. The voltage applied to the heaters varies from 20 to 90 V, and the corresponding heating power is in the range between 24 and 485 W. To record the temperature, we embed a thermistor beneath the surface of each plate. The thermistor has a room temperature resistance of 5 kΩ (Omega 44034) and is located near the centre of the plate. The upper side of the top plate is in contact with a cooling chamber, whose temperature is maintained by circulating cold water from a temperate-controlled bath/circulator. The temperature stability of the circulator is 0.01°C. To further increase the cooling power of the whole flow system, a flow-through cooler is connected in series to the downstream side of the cooling chamber. As shown in figure 1(*b*), cold water is fed into the chamber through two opposing inlets on the side of the chamber and flows out through two outlets on the top of the chamber.

As shown in figure 1(*a*), the two convection cells are identical except one has smooth upper and lower surfaces ('smooth cell') and the other has rough upper and lower surfaces ('rough cell'). To facilitate the construction of the rough cell, we fabricate a pair of identical rough surfaces from two separate brass plates and then attach them firmly onto the smooth top and bottom plates by small screws. Care has been taken to ensure that the smooth side of each rough plate is in good thermal contact

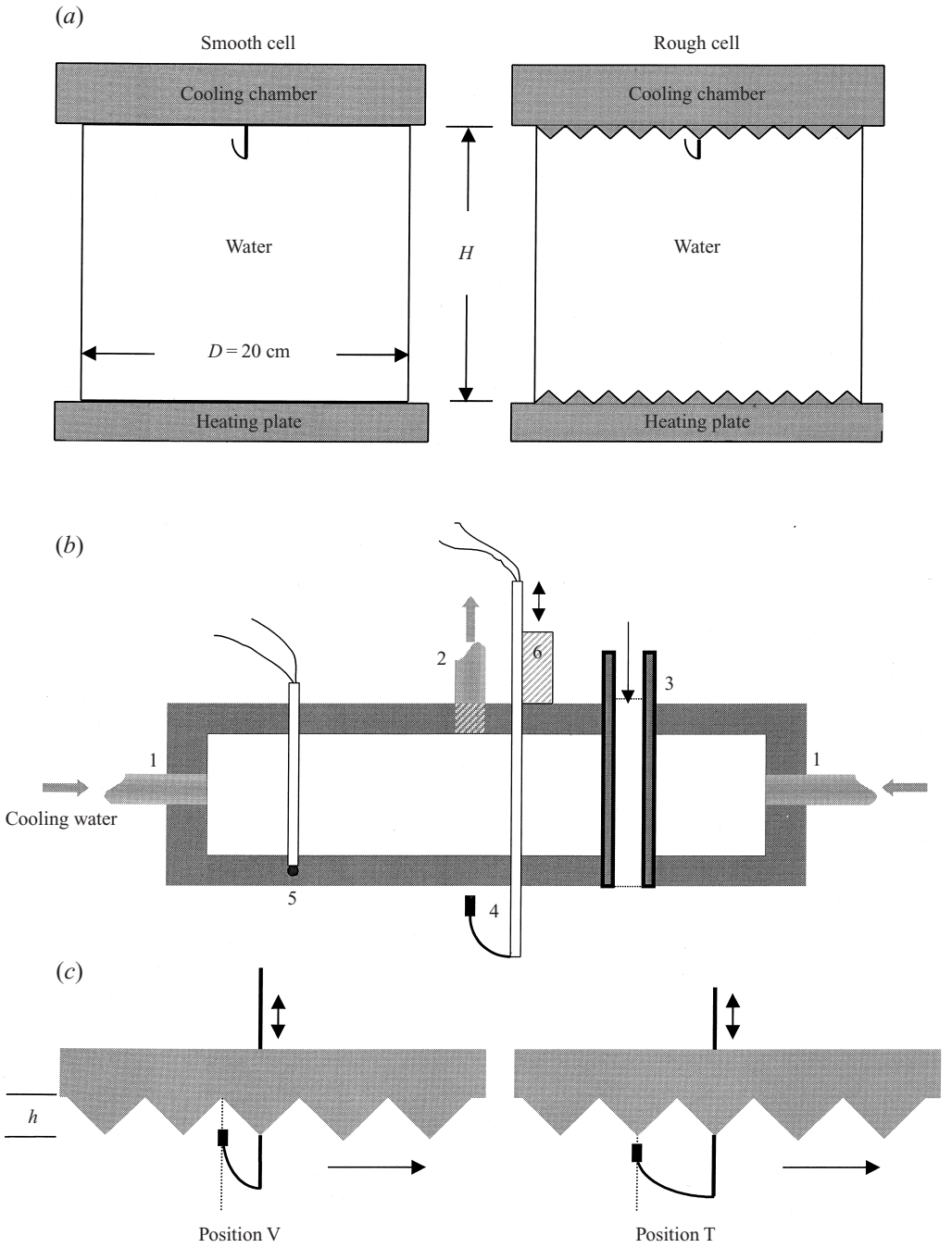

FIGURE 1. (*a*) Sketch of the convection cells used in the experiment. (*b*) Side view of the cooling chamber: 1, inlets; 2, outlets; 3, filling tube; 4, movable thermistor assembly; 5, top plate thermistor; 6, translation stage. (*c*) Two lateral positions of the movable thermistor in the rough cell. The horizontal arrow indicates the direction of the local flow.

with the substrate. The rough surface is made by woven V-shaped grooves and each of them has a vertex angle of 90°. The spacing between the grooves is such that a square lattice of pyramids is formed on the surface. The height of the pyramids (the roughness height h) is 9.0 mm and their spacing is $2h$. To compare the heat transport measurements, we also use another pair of rough surfaces that have the same surface structure but the roughness height is $h = 3.2$ mm. The height of the Plexiglas rings used for the rough cell is adjusted slightly, so that the base-to-base distance between the two opposing rough surfaces is the same as the height of the corresponding smooth cells. To accurately measure the surface temperature of the rough plates, we embed two additional thermistors on each rough plate. These thermistors are placed underneath the bottom of the grooves, so that the small boundary resistance between the rough plate and its substrate does not affect the measurement of the temperature difference ΔT across the bulk fluid. Because the vertical distance between the thermistor and the bottom of the groove is small (< 0.6 cm), the corresponding temperature drop in the rough plate is less than 3.5% of the measured ΔT.

A small movable thermistor (Thermometrics, AB6E3-B10KA202J) is installed inside the cell in order to measure the temperature of the convecting fluid. A thin stainless steel tube of diameter 1.1 mm is installed through the centre of the cooling chamber to guide the temperature probe and the connecting wires into the cell. The tube is mounted on a micrometer-controlled translation stage, so that the local temperature $T(z)$ of the fluid can be measured as a function of distance z away from the upper (cold) plate with an accuracy of 1 μm. In the rough cell, we measure the temperature profile $T(z)$ at two different lateral positions. As shown in figure 1(*c*), one position is directly below the tip of a central pyramid ('position T') and the other is inside the 'valley' in between the two crossing grooves at the centre of the top plate ('position V'). All the movable thermistors used in the experiment are calibrated individually with an accuracy of 0.01°C. Over the temperature range between 10°C and 45°C, the measured resistance of each thermistor is well described by the Steinhart–Hart equation: $1/T = a + b \ln R + c(\ln R)^3$, where T is the absolute temperature, R is the measured resistance of the thermistor, a, b, and c are the fitting parameters. This equation is used to convert the measured resistance to the local temperature with the calibrated values of a, b, and c for each thermistor.

2.2. *Experimental procedures*

Distilled water is used as the convecting fluid and is fed into the cell through a filling tube of 9.3 mm in diameter (see figure 1*b*). Prior to the temperature measurements, water is degassed by setting the cooling chamber at room temperature and the heating power supply at 90 V, which is the highest voltage used in the experiment. With the degas procedure, we remove all the air bubbles and they do not reappear later in the cell when different heating voltages are applied during the experiment. The whole convection cell is wrapped in three layers of thermal insulating rubber sheets to prevent heat leakage. In this way, all the heat produced by the bottom heating films is transferred through water to the top plate. The vertical heat flux is then calculated from the electric power required to keep the lower plate at a constant temperature. In the experiment, the temperature difference ΔT between the top and bottom plates varies from 4°C to 50°C depending on the heating power. By adjusting the temperature of the cooling water, we maintain the temperature of the bulk fluid at 30°C $\pm$ 1°C for all the measurements. The corresponding Prandtl number of the fluid is approximately 5.4. The temperature of the top and bottom plates is regulated within 0.1°C in standard deviation, which is less than 2.5% of ΔT.

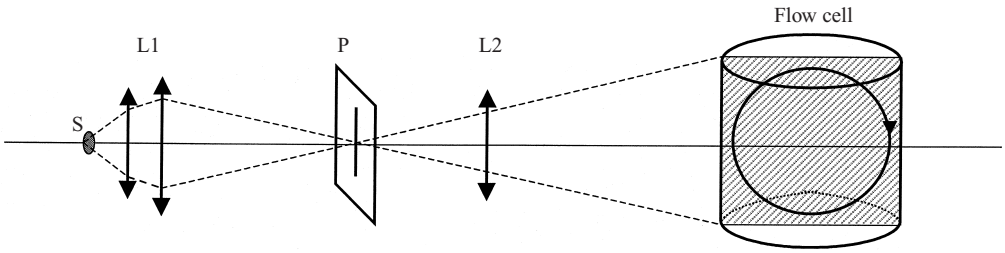

FIGURE 2. Schematic diagram of the optical set-up for flow visualization. S, GE quarzline lamp; L1, condensing lenses; P, adjustable slit; L2, collimating cylindrical lens.

A $7\frac{1}{2}$-digit multimeter (Keithley Model 2001) is used to measure the resistance of the movable thermistor. The resistance data, taken at a sampling rate of 20 Hz, are stored first in the memory of the multimeter and then transferred to a computer. A LabVIEW (National Instruments) program is composed to acquire a number of data files (typically 10–15 files) continuously into the computer. Each data file contains 29 899 readings, which is the maximum number allowed by the multimeter and corresponds to a continuous real-time measurement of 24.9 minutes. The transfer of each data file from the multimeter to the computer takes approximately 2 minutes. Because the duration of each continuous measurement is much longer than the correlation times in turbulent convection, the 2-minute gap between two consecutive files will not affect the statistical analysis of the measured temperature fluctuations. A separate digital multimeter is used to measure the temperature of the top and bottom plates, alternately, with a multi-channel mutiplexor on the back of the multimeter.

2.3. *Flow visualization*

To study the boundary layer dynamics in turbulent convection, we use a photographic technique to visualize the temperature and velocity fields near the boundary. With this technique, small thermochromic liquid crystal (TLC) spheres are seeded in the convecting fluid. These particles are composed of cholesteric liquid crystal and their Bragg scattered light changes colour from red to blue in a narrow temperature range. The TLC spheres used in the experiment are purchased from Hallcrest (Hallcrest, R29C4W) and they have been used previously in visualizing the temperature field of various flow systems (Adrian, Ferreira & Boberg 1986; Solomon & Gollub 1990; Zocchi, Moses & Libchaber 1990; Dabiri & Gharib 1991). These particles have a mean diameter of 15 μm and change colour from red to blue in the back-scattering direction over a temperature range of 4°C from 29°C to 33°C. The temperature of the bulk fluid is adjusted to be at 28.8°C, so that strong Bragg scattering can be seen from the side (at the scattering angle of 90°).

Figure 2 shows the optical set-up, which produces a thin sheet of white light for illuminating a vertical section of the convecting fluid. An overhead projector lamp (GE, ACG41-W3, 600W) is used as the light source (S). Two condensing lenses (L1) are used to collect the light from S and then project it onto an adjustable slit (P). The vertical sheet of light passing through the slit is focused onto the central section of the cell by a collimating cylindrical lens (L2). The thickness of the light sheet inside the cell is approximately 2 mm. The azimuthal orientation of the vertical light sheet is adjusted such that it coincides with the rotation plane of the large-scale circulation. It has been shown (Cioni *et al.* 1997) that the azimuth of the large-scale circulation rotates slowly inside the cylindrical cell when it is levelled perfectly. To

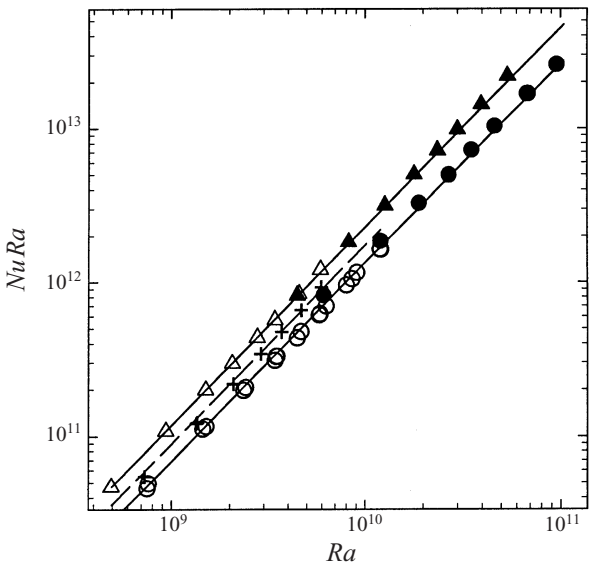

FIGURE 3. Measured $NuRa$ as a function of Ra in the smooth cells (circles) and in the rough cells with $h = 9.0$ mm (triangles). The solid symbols represent the data obtained from the cells with $A = 0.5$, and the open symbols are from the cells with $A = 1.0$. The solid lines are the power law fits. The pluses are obtained in another rough cell with $h = 3.2$ mm and $A = 1.0$. The dashed line is a power law fit to the pluses.

lock the azimuthal rotation of the large-scale circulation, we tilt the cell with a small angle of less than 2°. Ciliberto *et al.* (1996) have shown that such a small tilt does not affect turbulent convection very much. For flow visualization in the rough cell, we orientate the cell such that its central groove coincides with the rotation plane of the large-scale circulation. A Canon camera is used to take streak pictures of the TLC spheres with a long exposure time of 0.5 s. The streak picture can show the temperature and velocity fields simultaneously. In the picture of the TLC spheres, cooler regions of the fluid appear brown and warmer regions appear green and blue. We also use a colour CCD camera situated normal to the illuminating light sheet to get continuous images of the flowing TLC spheres and record them on a video tape with a S-VHS videocassette recorder.

3. Results and discussion

3.1. *Heat transport measurements and flow visualization*

In the study of thermal convection, the normalized heat flux across the cell is expressed by the Nusselt number $Nu = PH/(\pi R^2 k \Delta T)$, where P is the total heating power, ΔT is the resulting temperature difference across the fluid layer of thickness H, k is the thermal conductivity of the fluid, and πR^2 is the cross-sectional area of the cell. The control parameter in the convection experiment is the Rayleigh number $Ra = \alpha g H^3 \Delta T/(v\chi)$, where g is the gravitational acceleration, α, v and χ are, respectively, the thermal expansion coefficient, the kinematic viscosity, and the thermal diffusivity of the fluid. Because the heat transport measurement is conducted over varying heating power P, we plot the dimensionless heat flow $NuRa = P\alpha g H^4/(\pi R^2 k v \chi)$ as a function of Ra. In this way, one can minimize the errors introduced by the measurement of ΔT. Figure 3 shows the measured $NuRa$ as a function of Ra in the

smooth cells (circles) and in the rough cells with $h = 9.0\,\mathrm{mm}$ (triangles). The solid symbols represent the data obtained from the cells with the aspect ratio $A = 0.5$, and the open symbols are from the cells with $A = 1.0$. The measured $NuRa$ in the smooth cells is described well by the power law $NuRa = 0.17Ra^{1+\beta}$ (the lower solid line), which indicates $Nu = 0.17Ra^{\beta}$. The exponent $\beta = 0.29$ agrees well with the previous measurements in water (Chu & Goldstein 1973; Tanaka & Miyata 1980; Solomon & Gollub 1990; Cioni *et al.* 1997) and in low-temperature helium gas (Threlfall 1975; Heslot *et al.* 1987; Castaing *et al.* 1989). As shown in figure 3, the heat transport in the rough cells with $h = 9.0\,\mathrm{mm}$ is increased considerably in the whole range of Ra. For a fixed heating power P (i.e. at a fixed $NuRa$), the resulting temperature difference ΔT across the rough cell (and hence Ra) is found to be smaller than that across the smooth cell. This suggests that the rough cells have much less heat resistance than the smooth cells and thus are more efficient for heat transfer. The measured $NuRa$ in the rough cells can also be described by a power law with the same exponent β, but the amplitude is changed from 0.17 to 0.30 (the upper solid line). This amounts to a 76% increase in the heat transport. In the fitting we used all the data points available and ignored the small effect due to the different aspect ratio of the two convection cells. The conclusion remains the same if one uses only the data points from a single cell.

In a recent experiment, Shen *et al.* (1996) have shown that the effect of an ordered surface roughness on the heat transport depends on the length ratio δ/h, where δ is the thickness of the thermal boundary layer. In the small-Ra region, where $\delta > h$, the rough elements on the surface are buried beneath the thermal boundary layer, and hence the effect of the surface roughness is small. In the opposite limit of large Ra, where $\delta < h$, the surface roughness strongly affects temperature fluctuations near the surface and thereby alters the heat transport. Therefore, one expects a sharp transition in heat transport, which will occur when the Rayleigh number reaches a critical value Ra_c, where Ra_c is defined by the equation $\delta(Ra_c) \simeq h$. The boundary layer thickness $\delta(Ra)$ can be estimated by using the well-tested relation (Belmonte *et al.* 1995*a*) $\delta(Ra) = H/[2Nu(Ra)]$, where $Nu(Ra)$ is the measured Nusselt number as a function of Ra. Indeed, this transition in heat transport was observed by Shen *et al.* (1996). Recently, it was reconfirmed in a different experiment by Ciliberto & Laroche (1999). It was found that the measured heat flux in the rough cells remains the same as that in the smooth cells for small values of Ra. When Ra becomes larger than the transitional value Ra_c, the measured Nu starts to increase sharply (Shen *et al.* 1996). For the rough cells used in the present experiment with $h = 9.0\,\mathrm{mm}$, we have $Ra_c \simeq 1.8 \times 10^6$, which is far below the working range of Ra shown in figure 3. The pluses in figure 3 show the measured $NuRa$ in the rough cell with $h = 3.2\,\mathrm{mm}$ and $A = 1.0$. For this rough cell we have $Ra_c \simeq 6.4 \times 10^7$, which is slightly below the Ra range accessible to the present experiment. It is seen from figure 3 that the pluses deviate gradually from the circles at low Ra and then become parallel to the circles and triangles at higher values of Ra. Over a limited range of Ra, the pluses can also be described by a power law with the same exponent $\beta = 0.29$, but the amplitude is increased from 0.17 to 0.22 (the dashed line).

It should be pointed out that the enhanced heat transport in the rough cells cannot be explained by simple geometrical changes introduced by the rough surfaces, such as the effective contact area and height of the convection cell. There are several experimental results which do not support the contact area argument. (i) In the measurements shown in figure 3, we used two types of rough surfaces having the same surface geometry but different roughness height h (the spacing between the grooves is changed accordingly). The contact area of the two different types of rough

surfaces remains the same, but the measured $NuRa$ (or Nu) in the two rough cells differs considerably. For the cell with $h = 9$ mm, its heat transport is increased by 76%, whereas the heat transport in the cell with $h = 3$ mm is increased only by 29%. In both cases, the contact area of the rough surfaces is increased by 41% compared with the smooth surface. (ii) In a previous experiment, Shen *et al.* (1996) found that the enhanced heat transport in the rough cell occurs only when the Rayleigh number becomes larger than Ra_c. The measured heat flux in the rough cells remains the same as that in the smooth cells for smaller values of Ra, even though the contact area of the rough surface is still 41% more than the smooth surface. (iii) In a recent theoretical calculation, Villermaux (1998) considered the effect of a random rough surface with a broad distribution of length scales (a fractal-like rough surface) on the heat transport in turbulent convection. His model assumes that the net heat flux over a rough surface is proportional to the increase of the effective surface area and predicts that the scaling exponent β for Nu increases with the fractal dimension d_f of the random rough surface. The recent experiment by Ciliberto & Laroche (1999), however, shows the contrary. The above experiments suggest that the enhanced heat transport in the rough cell cannot be ascribed to the simple static changes in the contact area, rather it must be the local dynamics of the thermal boundary layer that changes the heat transport over the rough surface. As will be shown below, because of the non-uniform emission dynamics of the thermal plumes, the rough surface is no longer a homogeneous surface. The contact area argument, however, can apply only to a homogeneous surface.

We now discuss the effect of the cell height on the calculation of the heat transport in the rough cell. As shown in figure 3, the measured heat flux in the rough cells is described well by the power law $NuRa = BRa^{1+\beta}$ with $\beta = 0.29 \simeq \frac{2}{7}$. To estimate the effect of a height variation δH on the power-law amplitude B, we take differentiation on both sides of the equation and find that $\delta B/B = (1 - 3\beta)\delta H/H$. In figure 3, we used the base-to-base distance between the two opposing rough surfaces as the cell height H. If we use the tip-to-tip distance as the cell height, we have a maximum $\delta H/H = \frac{1.8}{20} = 9\%$ and the corresponding amplitude change $\delta B/B \simeq 1.3\%$. This is certainly a negligible effect. In fact, in the measurements shown in figure 3, we used two different rough cells with the aspect ratio $A = 1$ and $A = 0.5$, respectively. The corresponding value of $\delta H/H$ is changed by a factor of 2, but the measured $NuRa$ in both cells is found to obey the same power law without any change in the amplitude. Figure 3 thus demonstrates that the heat transport in the rough cell is not sensitive to variations of the cell height caused by the rough surfaces.

To find the real mechanism for the enhanced heat transport, we use the photographic technique described in § 2.3 to visualize the temperature and velocity fields near the upper rough surface. Figure 4(*b*) shows how a thermal plume (shown by an arrow) erupts from the (upper) cold rough surface. It is seen that the large-scale motion in the near-wall region is characterized well by a simple shear flow (from right to left). However, the mean flow is modulated by the rough surface, a situation very much like a steady flow passing over bluff obstacles on a wall (Faber 1995). The mean flow is forced to become divergent from the surface when it meets the upstream side of the pyramid. On the downstream side of the pyramid, an adverse pressure gradient region is formed inside the groove. This pressure gradient produces an eddy whose vorticity component is in the transverse direction to the mean flow and its sign is opposite to that of the large-scale circulation. The interaction between the upstream divergent flow and the downstream back-flow causes the thermal boundary layer to detach near the tip of the pyramid (see the sketch shown in figure 4*a*). The detached thermal

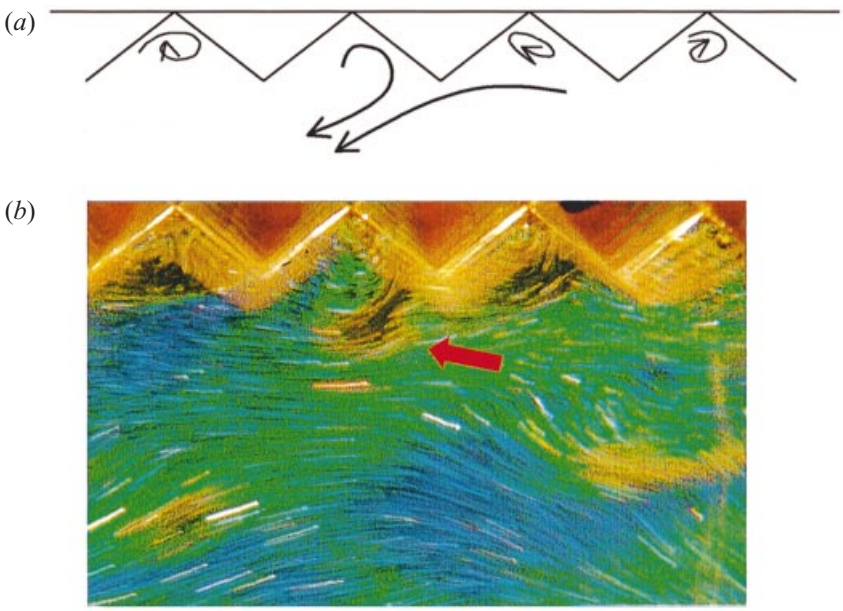

FIGURE 4. (*a*) Sketch of the flow field near the upper rough surface. (*b*) A typical streak image of the TLC spheres taken near the cold rough surface at $Ra = 2.6 \times 10^9$. The cold eruptions are brown; green and blue regions are warmer. The displayed region is approximately 7 cm by 4 cm. The arrow indicates a thermal plume, which has just erupted from the tip of the pyramid.

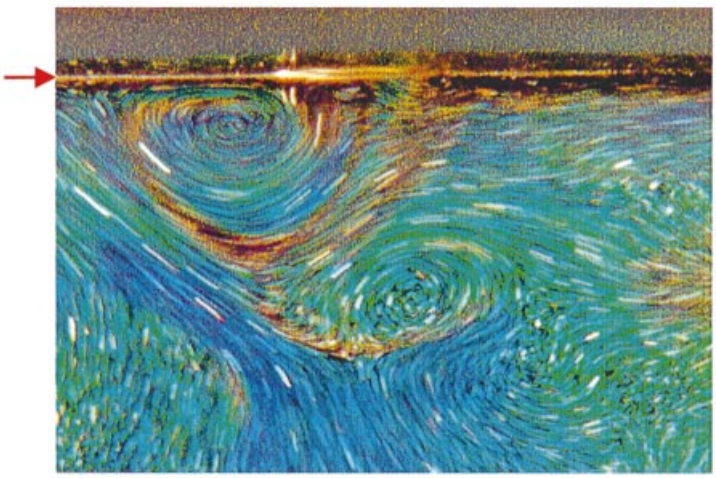

FIGURE 5. A streak image of the TLC spheres taken near the cold smooth surface at $Ra = 2.6 \times 10^9$. The mean flow direction is from right to left, so that the vortex pair is tilted to the left. The displayed region is approximately 6.5 cm by 4 cm. The arrow on the left side of the graph indicates the position of the upper smooth surface.

boundary layer becomes a thermal plume, which is sheared to the downstream by the mean flow. This situation is similar to the boundary layer separation from a rigid wall with a salient edge, which has been discussed in detail by Batchelor (1967).

Figure 5 shows a streak picture of the TLC spheres taken near the upper surface of the smooth cell at $Ra = 2.6 \times 10^9$. We find that the emission dynamics of the thermal

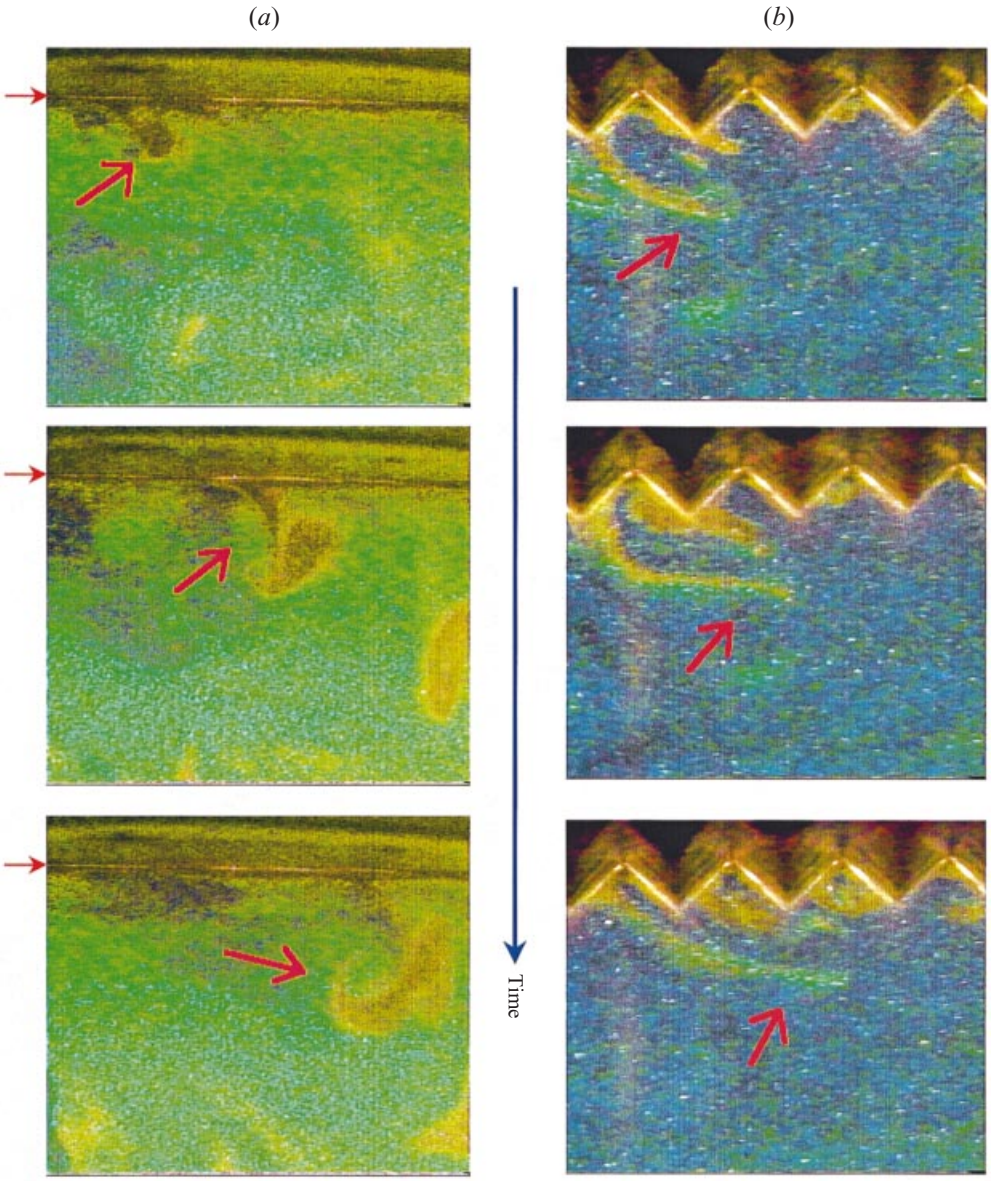

FIGURE 6. A time sequence of the TLC particle images illustrating the eruption process of a thermal plume (shown by a red arrow) (*a*) in the smooth cell and (*b*) in the rough cell at $Ra = 2.6 \times 10^9$. The time interval between two adjacent frames in (*a*) is 2 s and that in (*b*) is 1 s. The displayed region is approximately 6.5 cm by 4 cm.

plumes in the smooth cell is totally different from that in the rough cell. In the smooth cell, the thermal plume erupts by its own buoyancy force, which accelerates the fluid in the central stem of the plume. The sudden acceleration of the fluid produces a vortex ring around the stem (similar to the generation of a smoke ring), which gives the characteristic mushroom shape of the thermal plume. A two-dimensional projection of the vortex ring gives rise to a pair of vortices with opposite signs, which are clearly shown in figure 5. The vortex structure of the thermal plume shown in figure 5 is

a two-dimensional projection on the rotational plane of the large-scale circulation. Many years ago, Turner (1962) studied the shape of an isolated thermal plume and found a vortex ring solution for it. Recently, Moses, Zocchi & Libchaber (1993) carried out a detailed experimental study on the shape of the thermal plumes and found that to a large extent the thermal plumes in turbulent convection behave like the laminar plumes in a quiescent background. Our visualization measurements agree with these studies. In a recent visualization experiment, Zocchi *et al.* (1990) studied various coherent structures in turbulent convection, but their vortex dynamics has not been explored so far in great detail. Clearly, vorticity is an essential ingredient for describing the thermal plumes in turbulent convection and needs to be further studied. In the rough cell, however, we find that the interaction between the eddies trapped inside the groove and the large-scale circulation causes the detachment of the thermal boundary layer near the tip of the rough elements. Because the detachment of the boundary layer is driven by the large-scale flow instead of the buoyancy force, the vortex structure generated by the buoyancy acceleration disappears and thus the thermal plumes in the rough cell lose their mushroom cap. Occasionally, we do see a few mushroom-shaped thermal plumes in the rough cell (see Du & Tong 1998, figure 3), but the majority of the thermal plumes looks like that shown in figure 4(*b*).

Figure 6 shows the eruption process of a thermal plume (shown by a red arrow) in the smooth cell (figure 6*a*) and in the rough cell (figure 6*b*). The video images were first recorded on a S-VHS tape and then digitized into a computer. The cold eruptions are brown; green and blue regions are warmer. Because the convecting fluid in the two cells has a slightly different mean temperature, the two time series of images show different background colours. The arrow on the left side of the graphs in figure 6(*a*) indicates the position of the upper smooth surface (the bright line). The image above the bright line is caused by the reflection of the smooth surface. A thin fluid layer of brown colour near the smooth surface (the bright line) is the thermal boundary layer, which fluctuates with time. The top graph in figure 6(*a*) shows a thermal plume (shown by an arrow), which has just erupted from the cold surface. The initial shape of the 'plume cap' varies from time to time, and here it looks like a spherical blob. Because of the large-scale circulation, the thermal plume is sheared to the downstream direction (to the right). It is seen from the middle graph that after 2 s the thermal plume is shifted to the middle of the picture (travelling distance is $\sim$ 2.3 cm) and obtains the characteristic mushroom shape. As the thermal plume is further sheared to the downstream direction, the left-hand part of the plume, whose transverse vorticity component has the same sign as that of the large-scale circulation, gains more energy whereas the right-hand part of the plume, whose transverse vorticity component is opposite to that of the large-scale circulation, gradually loses its kinetic energy. Eventually, the right-hand part of the plume disappears and the left-hand part becomes part of the large-scale circulation. The bottom graph in figure 6(*a*) shows the thermal plume at the later stage.

Figure 6(*b*) shows the eruption process of a thermal plume in the rough cell. The top graph shows a brown thermal plume (shown by a red arrow), which has just erupted from the tip of the left-most pyramid. The thermal plume possesses a shape different from those in the smooth cell and does not have a mushroom cap. Similar to the situation in the smooth cell, the thermal plume is sheared to the downstream direction (to the right) by the large-scale circulation. It is seen from the middle graph (1 s later) that while the top part of the plume is sheared to the right, the 'root' is pinned down to the tip of the pyramid. This situation differs from that shown in figure 6(*a*), in which the root of the thermal plume is found to slide on the smooth surface when the

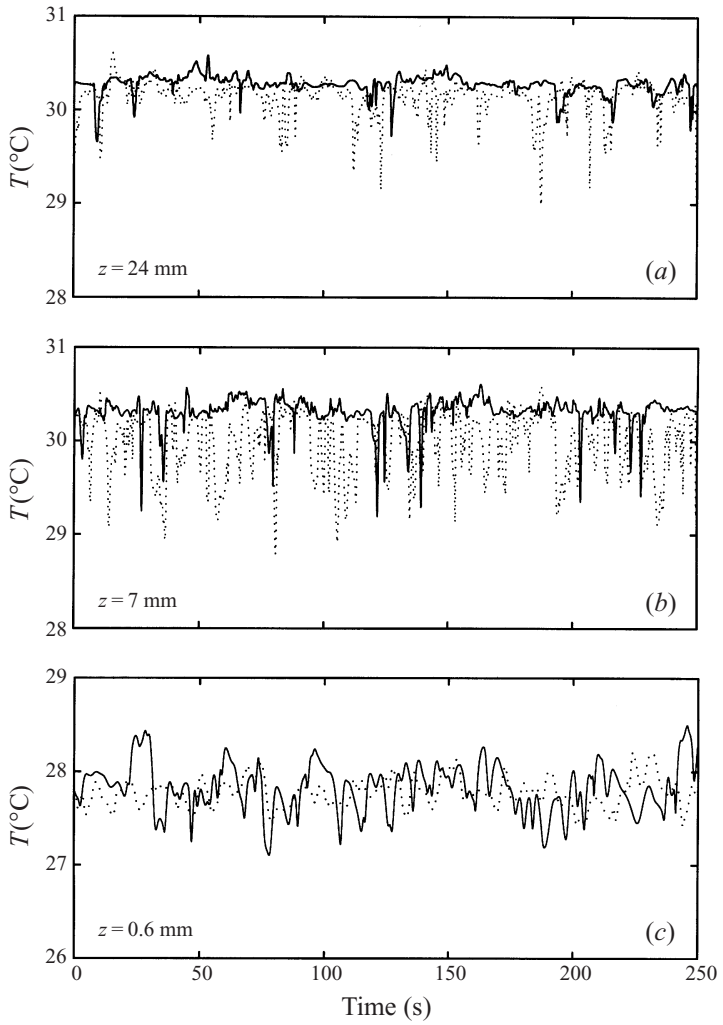

FIGURE 7. Typical time series measurements of temperature fluctuations near the upper (cold) plate in the smooth (solid curve) and rough (dotted curve) cells. The movable temperature probe in the rough cell is placed at the position V and the distance z is measured from the bottom of the groove.

whole plume is sheared to the right. The bottom graph in figure 6(*b*) shows the later stage of the thermal plume, which is further sheared to the right. The colour of the plume is changed from brown to light green after 2 s, indicating that heat has diffused into the cold plume and its temperature is increased. It is also seen from figure 6(*b*) that more thermal plumes erupt from the nearby pyramids just after the emission of the first one. Such a multiple emission process is observed in the rough cell sometimes, but we have not systematically studied the sequencing and correlation between the eruptions. All the visualization measurements reported in this section were conducted at a fixed roughness wavelength ($2h$). Certainly, the eruption dynamics of the thermal plumes in the rough cells with different lateral surface structures is interesting and needs to be further studied. In the above discussion, we focused our attention on the eruption process of an individual plume.

3.2. *Local temperature fluctuations and their histograms*

The visualization measurements discussed above reveal the global structure of the temperature and velocity fields near the upper rough surface. We now discuss the local temperature measurements in this region, which provide statistical information about the temperature fluctuations. All the local temperature measurements, to be discussed in this and the following sections, are performed in the cells with $A = 1$. Figure 7 shows typical time series measurements of the local temperature T in the smooth (solid curve) and rough (dotted curve) cells. The measurements are made at $Ra = 1.5 \times 10^9$ and the corresponding thermal boundary layer thickness is $\delta \simeq 1.5$ mm. The movable temperature probe in the rough cell is placed at the position V and the distance z is measured from the bottom of the groove. The values of z are: (*a*) $z = 24$ mm (outside the rough surface), (*b*) $z = 7$ mm (inside the groove but outside the thermal boundary layer), and (*c*) $z = 0.6$ mm (inside the thermal boundary layer). It is seen from figure 7 that the cold fluctuations are superposed on an average base line. The downward going spikes are associated with cold plumes detached from the upper boundary layer and they are carried through the temperature probe by the large-scale circulation. Figure 7(*b*) clearly shows that the emission frequency of the (cold) thermal plumes is increased greatly in the rough cell. From the flow visualization we have learned that near the upper rough surface many thermal plumes are carried away horizontally by the large-scale circulation. Therefore, moving the temperature probe further away from the boundary will reduce the probability of detecting the thermal plumes. Nevertheless, figure 7(*a*) shows that there are still some energetic thermal plumes, which can penetrate vertically into the bulk region of the convective flow.

To learn the distribution of the temperature fluctuations, we compute their histogram using the time series data. The temperature fluctuation is defined as $\delta T = T - \bar{T}$, where $\bar{T}$ is the average local temperature. Figure 8 shows the temperature histograms corresponding to the time series measurements shown in figure 7. The duration of the time series measurement was set to be 8.3 minutes (10 000 data points) for each value of z and the sampling rate was 20 Hz. It is seen from figure 8(*a*) that when z is far away from the boundary ($z = 24$ mm), the temperature histograms for the smooth and rough cells have a similar shape. Both of them are skewed towards the cold side, because more cold plumes are captured in the time series measurements. As shown in figure 7(*a*), the emission frequency of the cold plumes is increased in the rough cell and, therefore, the corresponding histogram has a wider distribution when compared with that in the smooth cell. In the groove region ($z = 7$ mm), the measured histogram shows a bigger shoulder on the cold side, which suggests that the extra thermal plumes produced by the rough surface are mostly of medium size. From the flow visualization we have learned that the interaction between the horizontal shear flow and the rough surface creates small eddies in the groove region. These eddies produce a strong mixing effect, which increases temperature fluctuations on both the warm and cold sides. This is clearly shown in figure 8(*b*). In contrast to the situation at $z = 7$ mm, temperature fluctuations inside the boundary layer ($z = 0.6$ mm) are found to be reduced in the rough cell. Figure 7(*c*) shows that these temperature fluctuations are more symmetric and do not have sharp spikes as those shown in figures 7(*a*) and 7(*b*). It is seen from figure 8(*c*) that the temperature fluctuations deep inside the groove region are reduced considerably when compared with those in the smooth cell. As will be shown in the next section, the thermal boundary layer thickness δ is increased in the groove region. These measurements suggest that the thermal boundary layer in the groove region is further stabilized by the enhanced detachment of the thermal plumes near the tip of the pyramids.

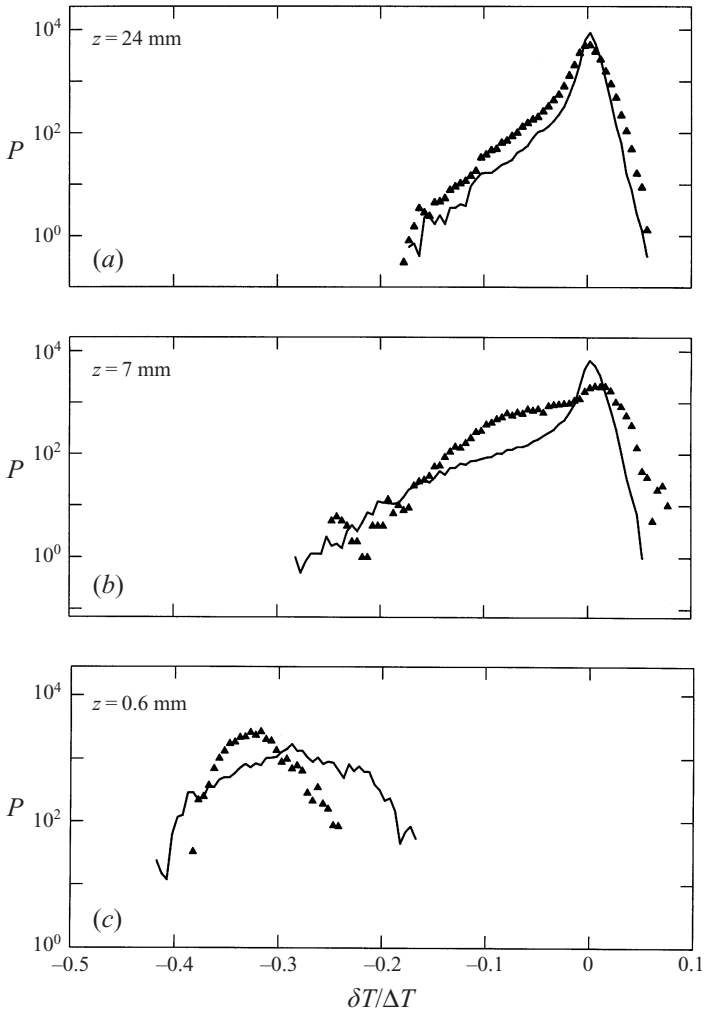

FIGURE 8. Comparison of the temperature histograms between the smooth (solid curves) and rough (triangles) cells. The histograms are computed using the time series data shown in figure 7.

Because the local heat transport is inversely proportional to δ, one might ask why the overall heat transport is increased whereas the local temperature gradient in the groove region is reduced? To answer this question, we measure the temperature fluctuations near the tip of a central pyramid. Figure 9 compares the temperature fluctuations at the position V (dotted curve) and position T (solid curve). The corresponding histograms are shown in figure 10. Figure 9(*a*) shows the time series measurements when z is at 24 mm away from the bottom of the groove (dotted curve) and at 14 mm away from the tip of the pyramid (solid curve). Because the height of the pyramid is 9 mm, the two measurements are made at approximately the same horizontal level far away from the rough surface. The measured histograms clearly show that the temperature fluctuations at this distance are independent of the horizontal position. The situation is changed completely, when the distance z is closer to the rough surface. In figure 9(*b*), the dotted curve is measured at 7 mm away from the bottom of the groove (slightly inside the groove) and the solid curve

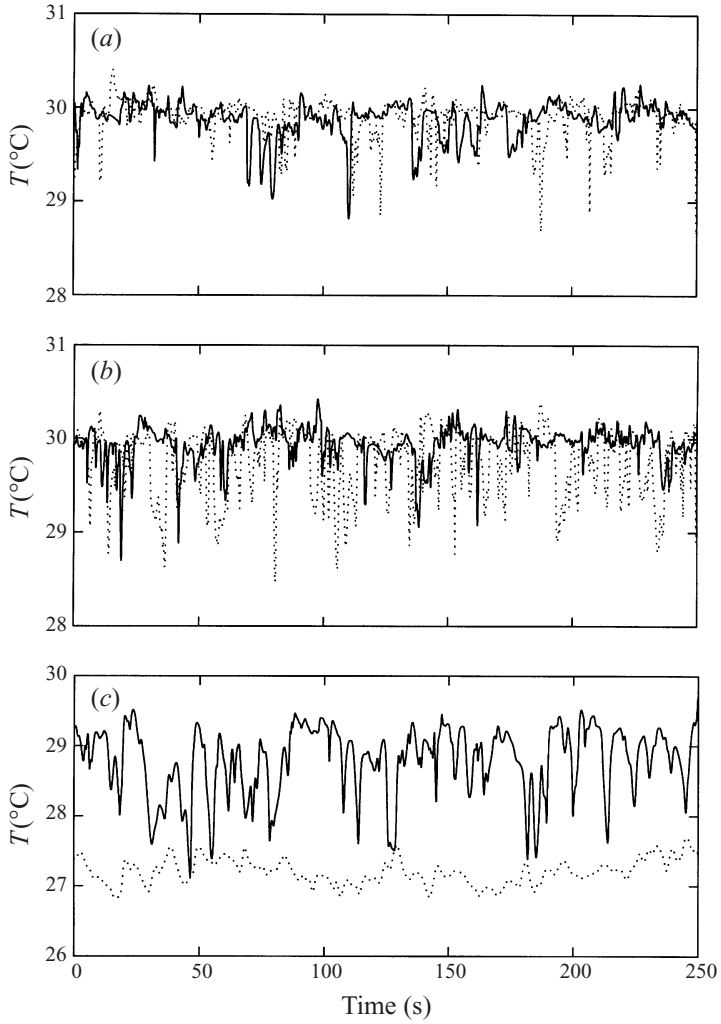

FIGURE 9. Time series measurements of the temperature fluctuations at the position V (dotted curve) and position T (solid curve). The measurements are made at $Ra = 1.5 \times 10^9$. The values of z for the solid curves are: $z = 14$ mm (a), 7 mm (b), and 0.6 mm (c). The values of z for the dotted curves are: $z = 24$ mm (a), 7 mm (b), and 0.6 mm (c). The distance z at the two lateral positions T and V are measured, respectively, from the tip of the pyramid and from the bottom of the groove.

is measured at 7 mm away from the tip of the pyramid (outside the groove). It is seen from figures 9(b) and 10(b) that there are more downward spikes at the position V. From the visualization measurements discussed in the last section, we have learned that most thermal plumes emitted near the tip of the rough elements are sheared horizontally to the downstream by the mean flow and some of them are even mixed into the groove region by the eddies trapped inside the grooves. As a result, more thermal plumes are found in the horizontal plane with a vertical height comparable to the tip height h, and fewer plumes are detected in the horizontal plane far above the tip. From both the local and global temperature measurements, we conclude that the main effect of the surface roughness is to increase the emission of the thermal plumes near the tip of the rough elements. These extra thermal plumes are responsible for the enhanced heat transport shown in figure 3.

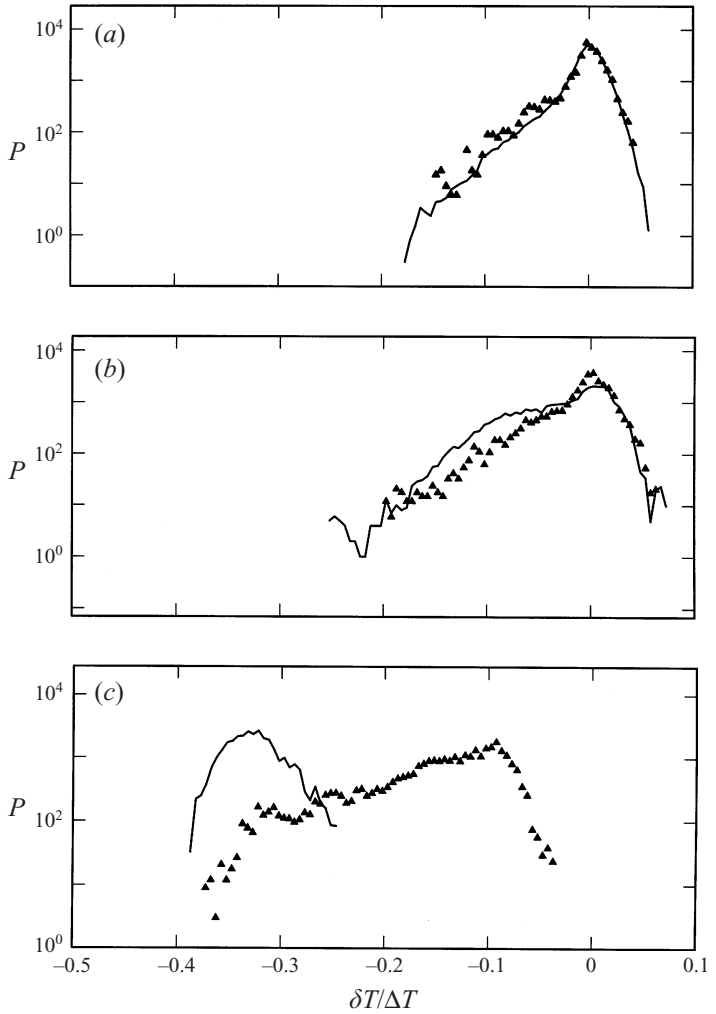

FIGURE 10. Comparison of the temperature histograms at the position V (solid curve) and position T (triangles). The histograms are computed using the time series data shown in figure 9.

Figures 9(*c*) and 10(*c*) show the temperature fluctuations and their histograms when z is inside the thermal boundary layer. An important feature shown in figure 9(*c*) is that the average surface temperature at the tip is higher than that at the bottom of the groove. Unlike the smooth surface, the rough surface is no longer isothermal under the uniform heating. The pyramids are surrounded by warm water and emit more cold plumes near the tip. This non-uniform boundary layer dynamics destroys the surface homogeneity and produces a higher surface temperature at the tip. It should be pointed out that the surface temperature difference between the tip and groove cannot be simply ascribed to the relatively small thermal conductivity of the brass plates used in the experiment. We believe that this lateral surface inhomogeneity is a general feature for turbulent heat transport over a rough surface, so long as the time scales associated with the boundary layer dynamics are shorter than the thermal diffusion time between the tip and groove over the solid plate. This is the case for the rough brass plates used in the present experiment and is also true for

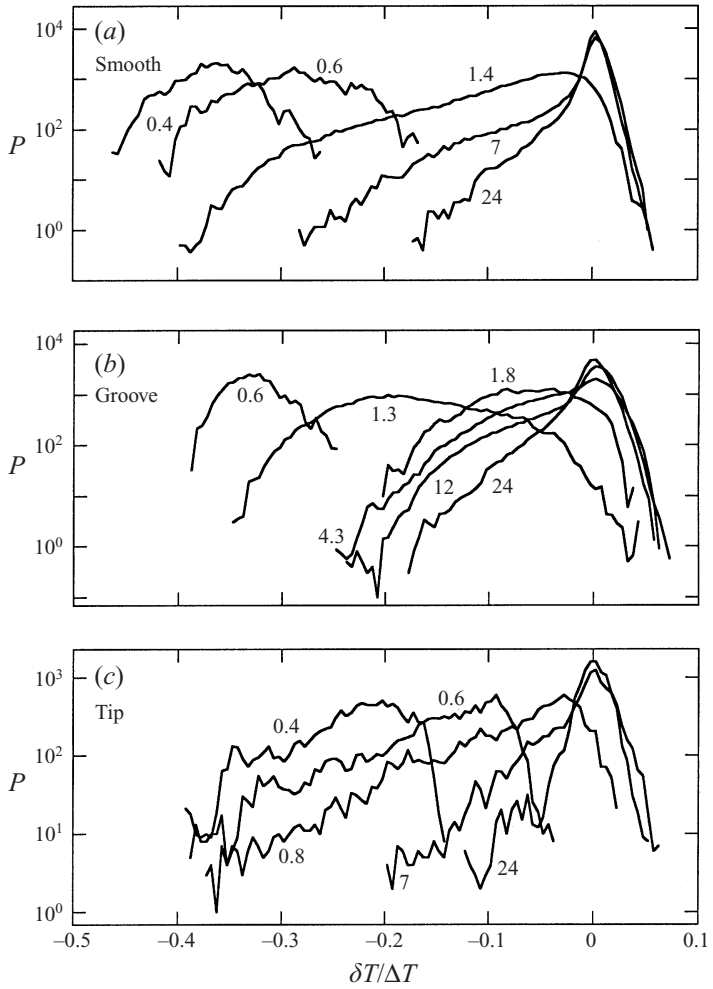

FIGURE 11. Measured temperature histograms at different values of z away from the top plate. The number near each curve indicates the value of z in mm. In the rough cell, the value of z at the position V (b) is measured from the bottom of the groove and at the position T (c) it is measured from the tip of the pyramid.

an even better thermal conductor, such as copper, whose thermal diffusion time is of the order of 1 s whereas the time scales associated with the temperature fluctuations near the boundary can be down to 0.07 s (15 Hz). It is seen from figure 9(c) that the temperature fluctuations near the tip are much stronger than those in the groove region. The temperature histogram near the tip is found to be skewed towards the cold side (i.e. the skewness $S \equiv \langle (T - \overline{T})^3 \rangle / \langle (T - \overline{T})^2 \rangle^{3/2} < 0$). This is because the large-scale circulation carries many cold plumes horizontally near the tip. At the bottom of the groove, however, the thermal boundary layer is influenced strongly by the eddy mixing effect, which produces more warm fluctuations inside the boundary layer. As a result, the temperature histogram shows a small positive skewness. These changes in the histogram are shown in figure 10(c). Note that the temperature histogram in the smooth cell is symmetric and its skewness S is approximately equal to zero.

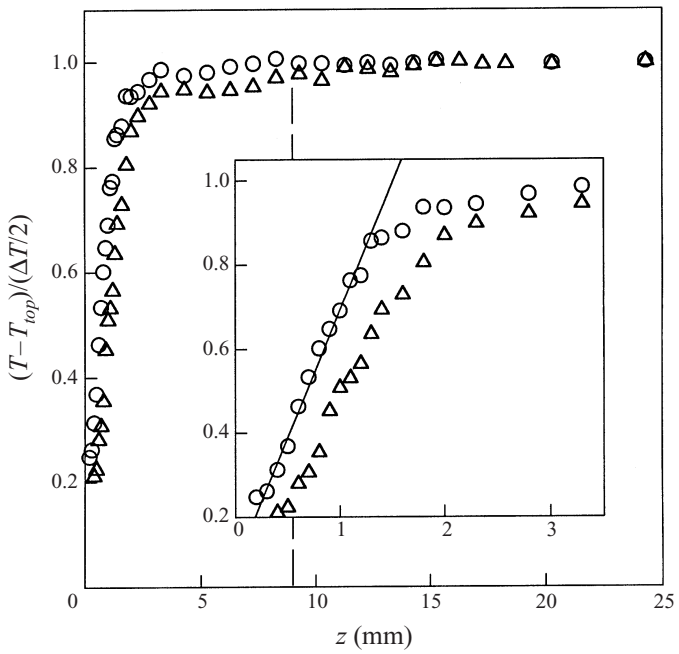

FIGURE 12. Measured mean temperature profile $T(z)$ in the smooth cell (circles) and in the rough cell at the position V (triangles). The measurements are made at $Ra = 1.5 \times 10^9$. The mean temperature, $T - T_{top}$, relative to the top plate temperature T_{top} is normalized by one half of the temperature difference ΔT across the cell. The vertical dashed line indicates the roughness height h. The insert shows an enlarged portion of the plot near the boundary and the solid line is a linear fit.

To further illustrate the changes of the temperature statistics at different z, we plot, in figure 11, the temperature histograms measured at different values of z in the smooth cell (a) and in the rough cell at the position V (b) and position T (c). The temperature histogram undergoes many changes in shape when z is varied from 0 to 100 mm (the centre of the cell). In the smooth cell, the shape of the histogram changes from a nearly Gaussian form within the boundary layer ($z = 0.4$ mm) to an exponential form (not shown in figure 11a) at the cell centre, with the broadest distribution at the edge of the thermal boundary layer ($z = 1.4$ mm). In the rough cell, the temperature histograms at the positions V and T undergo similar changes to those in the smooth cell, but they also show some interesting new features. As discussed above, the temperature histograms inside the thermal boundary layer have different skewness S. In the smooth cell, the distribution is symmetric and $S \simeq 0$. In the rough cell, however, the distribution becomes asymmetric and S changes its sign from a positive value at the position V to a negative value at the position T. Because the mean temperature inside the (cold) thermal boundary layer increases linearly with z, the peak position of the measured histograms changes with z until z becomes larger than the boundary layer thickness δ. From figure 11 we find that the edge of the boundary layer is located, respectively, at $z \simeq 1.4$ mm (a), 1.8 mm (b), and 0.8 mm (c). Figure 11 thus suggests that the value of δ is increased in the groove region, whereas near the tip of the pyramid δ is decreased when compared with that in the smooth cell.

3.3. *Temperature profiles near the upper surface*

To quantitatively characterize the temperature statistics at different values of z, we discuss, in this subsection, two important parameters of the temperature histogram. One is the mean temperature profile $T(z)$ and the other is the root mean square (RMS) temperature profile $T_{RMS}(z)$. Figure 12 shows the measured $T(z)$ near the top plate in the smooth cell (circles) and in the rough cell at the position V (triangles). The mean temperature at each value of z is obtained from the time series data and is normalized such that the top plate temperature is 0 and the bulk fluid temperature is 1. In the smooth cell, the measured $T(z)$ increases linearly with z for small values of z (the solid line in the insert). After it reaches a maximum value T_m, the measured $T(z)$ remains constant throughout the bulk region. The measurement indicates that turbulent mixing creates, on average, isothermal fluid in the bulk region and the temperature gradient across the cell is concentrated in thin thermal boundary layers. The boundary layer thickness δ can be defined as the distance at which the extrapolation of the linear part of $T(z)$ equals T_m. From figure 12 we find $\delta = 1.5$ mm in the smooth cell.

The temperature profiles measured in the rough cell at the positions V and T have a similar shape to that in the smooth cell, but they also show some interesting new features. It is seen from figure 12 that the mean temperature in the groove region ($z < h$) is reduced approximately by 0.5°C when compared with the smooth cell. This is caused by the mixing effect of the eddies trapped inside the cold groove. Another interesting feature shown in figure 12 is that the thermal boundary layer at the bottom of the groove becomes thicker than that in the smooth cell. The measured value of δ ($= 2.0$ mm) at the position V is increased by 33% at $Ra = 1.5 \times 10^9$. Because the local heat transport is proportional to δ^{-1} (Belmonte *et al.* 1995*a*), figure 12 thus suggests that the local heat transport in the groove region is reduced. The local heat transport near the tip, on the other hand, is found to be increased greatly. As shown in figure 13, the measured $T(z)$ near the tip has a shape similar to that in the smooth cell, but the value of δ is reduced from 1.5 to 0.85 mm. Figures 12 and 13 also show that the surface temperature at the tip (extrapolated to $z = 0$) is higher than that at the bottom of the groove. As discussed in the last section, the non-uniform emission dynamics of the thermal plumes destroys the temperature homogeneity on the rough surface. The local temperature measurements shown in figures 12 and 13 further support our conclusion that the interaction between the eddies trapped inside the groove and the large-scale circulation enhances the detachment of the thermal boundary layer near the tip of the rough elements. The measurements of $T(z)$ in the rough cell also indicate that the thermal boundary layer follows the contour of the rough surface. Figure 14 depicts a sketch of the thermal boundary layer near the rough surface.

We now examine how the temperature profile $T(z)$ changes with the Rayleigh number. It is found that the measured $T(z)$ in the smooth cell for different values of Ra can all be brought into coincidence, once the distance z is scaled by the thermal boundary layer thickness δ. The plot of $T(z)$ vs. z/δ remains invariant and only δ changes with Ra. Figure 15(*a*) shows the measured $T(z)$ as a function of z/δ for three different values of Ra in the smooth cell. The scaling behaviour of $T(z)$ suggests that the structure of the turbulent temperature field near the boundary is invariant with Ra. Similar scaling behaviour has been observed previously in a smooth cell filled with high-pressure gases (Belmonte *et al.* 1993). Figure 15(*b*) shows the measured $T(z)$ as a function of z for three different values of Ra in the rough cell at the position T. The shape of the measured $T(z)$ is similar to that in the smooth cell, but the value of δ now becomes insensitive to Ra. A possible reason for the Ra-independent

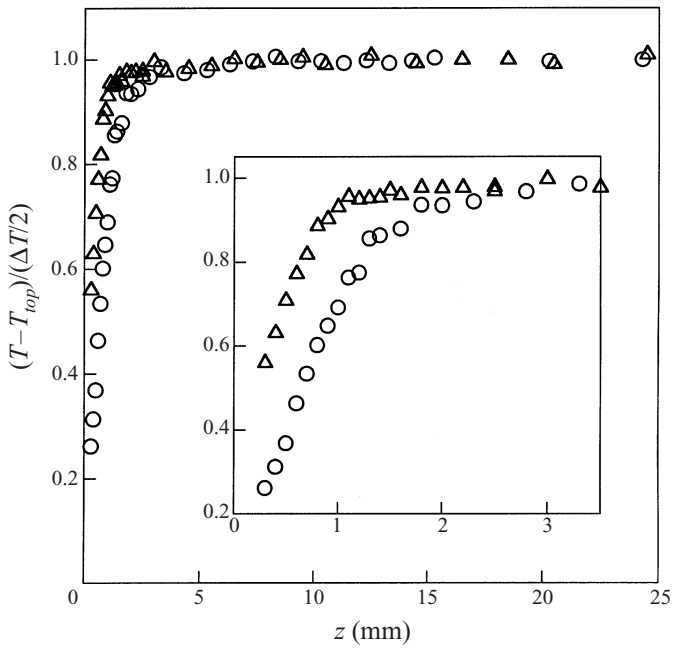

FIGURE 13. Measured mean temperature profile $T(z)$ in the smooth cell (circles) and in the rough cell at the position T (triangles). The measurements are made at $Ra = 1.5 \times 10^9$. The insert shows an enlarged portion of the plot near the boundary.

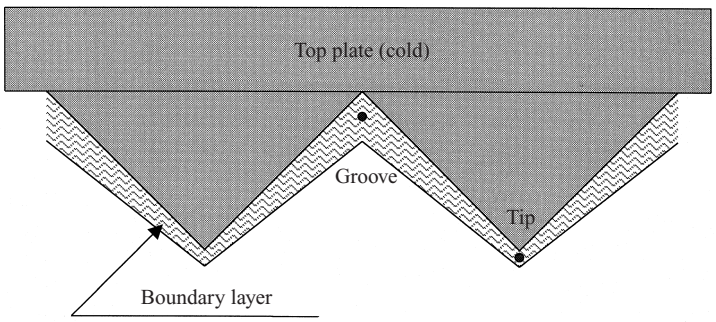

FIGURE 14. Sketch of the thermal boundary layer (wavy-lined area) near the rough surface. The small dots indicate the two probe positions used in the local temperature measurements.

behaviour of δ is that the thermal boundary layer may not be well developed at the tip, because it is a singular point on the rough surface. Figure 16 shows the measured $T(z)$ as a function of z/δ for three different values of Ra in the rough cell at the position V. The measured $T(z)$ near the boundary is found to scale with z/δ, but the shoulder part of $T(z)$ does not scale with z/δ. It has been shown in figure 12 that the small eddies trapped inside the groove reduce the mean temperature in the groove region ($z < h$) by ~ 0.5°C. Therefore, the shoulder part of $T(z)$ should scale with the roughness height h, which is independent of Ra. The h-scaling is indeed observed in the groove region and is shown in the insert of figure 16.

The surface roughness affects not only the mean temperature profile $T(z)$ but also the RMS profile $T_{RMS}(z)$. Figure 17 compares the measured $T_{RMS}(z)$ in the smooth cell (circles) with those in the rough cell at the position V (triangles in figure 17*a*)

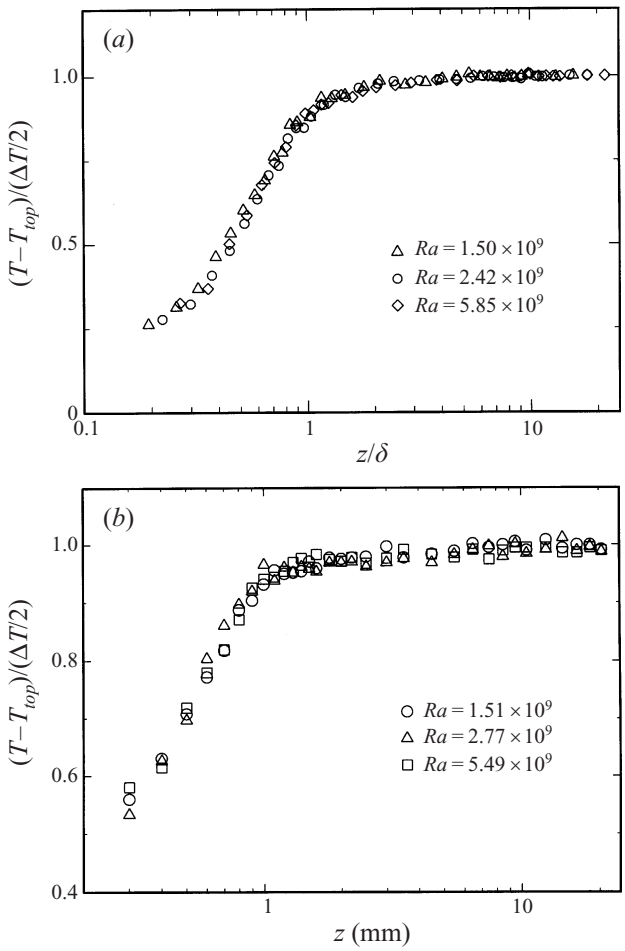

FIGURE 15. (*a*) Measured temperature profile $T(z)$ as a function of z/δ for three different values of *Ra* in the smooth cell. (*b*) Measured $T(z)$ as a function of z for three different values of *Ra* in the rough cell at the position T.

and position T (triangles in figure 17*b*). To view the near-wall portion of $T_{RMS}(z)$ more clearly, we use a logarithmic scale for z. The RMS profile is obtained from the time series measurements using the equation $T_{RMS}(z) = \langle (T(z) - \overline{T})^2 \rangle^{1/2}$, where $\overline{T}$ is the average local temperature. It is seen from figure 17 that the measured $T_{RMS}(z)$ has a well-defined peak located at the edge of the thermal boundary layer, suggesting that the boundary layer is a strongly fluctuating structure. Indeed, this has been observed in the flow visualization. The value of $T_{RMS}(z)/\Delta T$ peaks at $\sim 7\%$ and decays gradually to a value of $\sim 1\%$ at the centre of the cell. As shown in figure 17(*a*), the shape of the measured $T_{RMS}(z)$ near the tip is similar to that in the smooth cell, but the peak position is shifted toward the boundary. This is because the thermal boundary layer near the tip is thinner than that in the smooth cell.

The triangles in figure 17(*b*) show the measured $T_{RMS}(z)$ in the groove region. The peak position of $T_{RMS}(z)$ is shifted away from the boundary, because the boundary layer in the groove region is thicker than that in the smooth cell. As discussed in the previous section, the small eddies trapped inside the groove produce a strong mixing

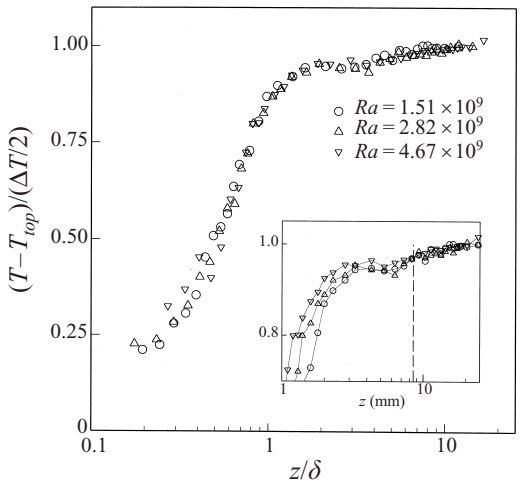

FIGURE 16. Measured temperature profile $T(z)$ as a function of z/δ for three different values of Ra in the rough cell at the position V. The insert shows the same plot as a function of z.

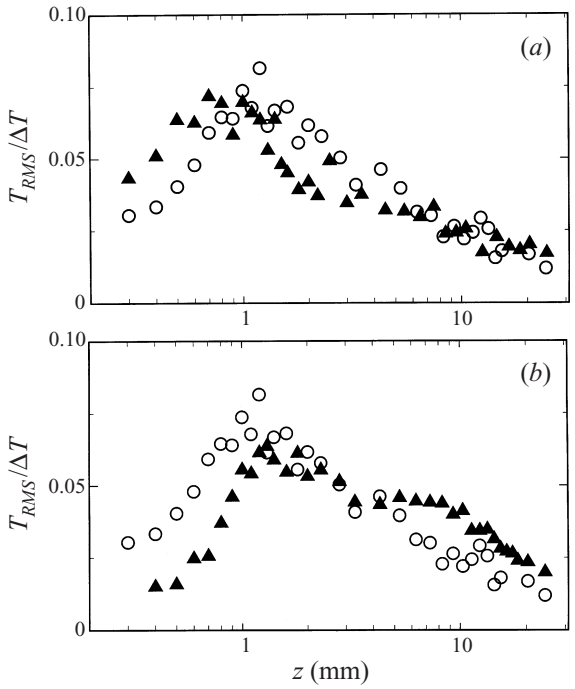

FIGURE 17. (*a*) Measured RMS profile $T_{RMS}(z)$ in the smooth cell (circles) and in the rough cell at the position T (triangles) with $Ra = 1.5 \times 10^9$. $T_{RMS}(z)$ is normalized by the temperature difference ΔT. (*b*) Measured $T_{RMS}(z)$ in the smooth cell (circles) and in the rough cell at the position V (triangles) with $Ra = 1.5 \times 10^9$.

effect, which creates large temperature fluctuations. It is seen from figure 17(*b*) that the measured $T_{RMS}(z)$ inside the groove region ($z < h$) is increased by more than 100%. Another interesting feature shown in figure 17(*b*) is that the influence of the surface roughness extends way into the bulk region, in which the measured T_{RMS} is

still considerably larger than that in the smooth cell. From measurements at the centre of the rough cell (Du & Tong 2000), we find that the temperature histogram retains the same exponential form as that in the smooth cell and the measured $T_{RMS}/\Delta T$ obeys the same $Ra^{-1/7}$ scaling law. However, the power-law amplitude in the rough cell is increased by $\sim 35\%$. It becomes clear now that the rough elements on the surface play an important role in the emission dynamics of the thermal plumes. Rather than simply sheltering the groove region from the large-scale circulation, the rough elements help to create a secondary flow (eddies) in the groove region. This secondary flow together with the large-scale circulation enhance the detachment of the thermal boundary layer near the tip of the pyramids. In the groove region, the secondary flow produces a strong eddy mixing effect, which suppresses the emission of the thermal plumes and at the same time creates large temperature fluctuations outside the thermal boundary layer.

We now discuss the *Ra*-dependence of $T_{RMS}(z)$. Figure 18 shows the measured $T_{RMS}(z)$ in the smooth cell (*a*) and in the rough cell at the position T (*b*) and position V (*c*) for different values of *Ra*. Similar to the mean temperature profile $T(z)$, the RMS profile $T_{RMS}(z)$ in the smooth cell also scales with δ. As shown in figure 18(*a*), plots of $T(z)$ vs. z/δ for different *Ra* remain invariant and only δ changes with *Ra*. The value of $T_{RMS}(z)/\Delta T$ peaks at $\sim 7\%$ and does not change very much with *Ra*. The measured $T_{RMS}(z)/\Delta T$ outside the boundary layer decreases with increasing z and can be fit to a function $T_{RMS}/\Delta T \sim \ln z$. Experimental uncertainties for $T_{RMS}(z)$ are largely statistical due to the relatively short duration of the time series measurements. The measured $T_{RMS}(z)$ in water agrees well with the previous measurements in a smooth cell filled with high-pressure gases (Belmonte *et al.* 1995*a*). The scaling behaviour of the measured $T_{RMS}(z)$ suggests that the temperature fluctuations in the smooth cell of aspect ratio one are controlled by a universal mechanism.

The RMS profiles measured in the rough cell have a similar scaling behaviour to those in the smooth cell. Figure 18(*b*) shows the measured $T_{RMS}(z)$ in the rough cell at the position T. Since the boundary layer thickness near the tip does not change very much with *Ra*, we plot the measured $T_{RMS}(z)$ as a function of z instead of z/δ. Because temperature fluctuations near the tip are strong and the thermal boundary layer is very thin, it becomes difficult to determine δ accurately and the RMS data have relatively large statistical uncertainties near the tip. Nevertheless, one can still see from figure 18(*b*) that the RMS profiles for different *Ra* have a similar shape to those in the smooth cell. As discussed above, the temperature fluctuations in the groove region are enhanced greatly because of the eddy mixing effect. It is seen from figure 18(*c*) that the measured $T_{RMS}(z)/\Delta T$ reaches a maximum value of 7% at the edge of the thermal boundary layer, remains at a constant value of 4% throughout the groove region, and then decreases with further increasing z outside the rough surface. The shape of the measured $T_{RMS}(z)$ for different *Ra* remains unchanged and only δ changes with *Ra*. The fact that the measured $T_{RMS}(z)$ remains constant inside the groove region ($z < h$) suggests that the small eddies trapped in the groove region are very effective in homogenizing the temperature fluctuations in the region. These findings further confirm that the small eddies play an important role in the boundary dynamics near the rough surface.

4. Conclusion

We have carried out a systematic study of turbulent thermal convection in a cell with rough upper and lower surfaces. Flow visualization and heat transport

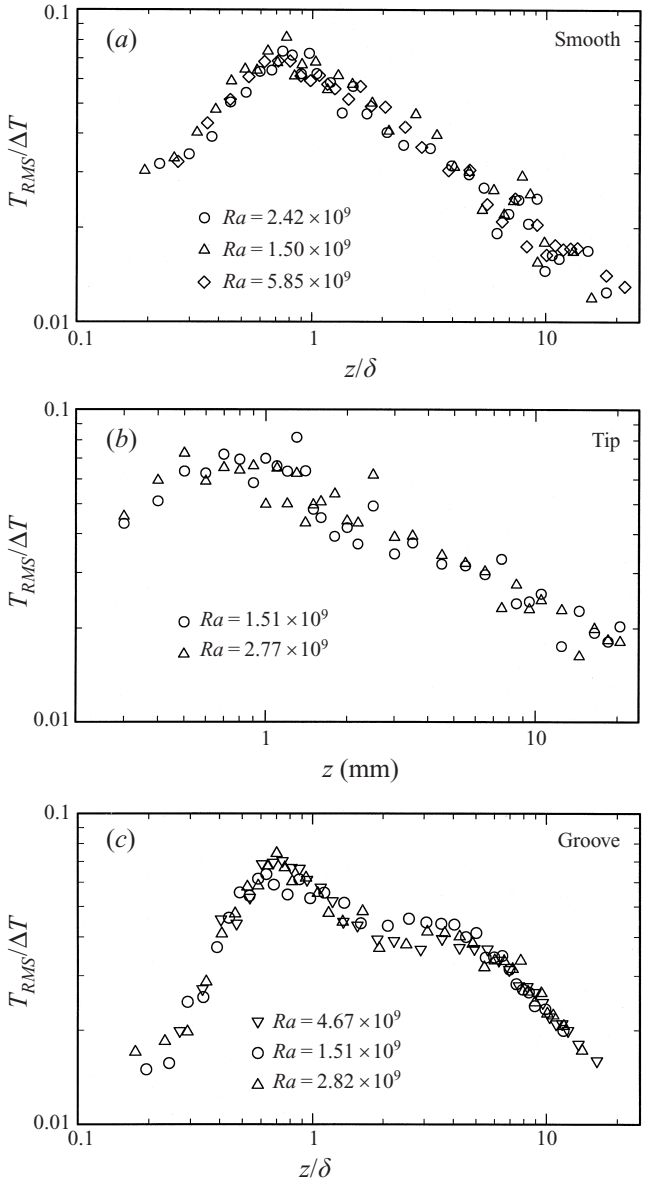

FIGURE 18. Measured $T_{RMS}(z)/\Delta T$ in the smooth cell (*a*) and in the rough cell at the position T (*b*) and position V (*c*) for different values of *Ra*.

measurements are performed in the rough cell and the results are compared with those in the smooth cell. The measured heat flux in the rough cell is found to obey the same $Ra^{2/7}$ scaling law as that in the smooth cell but the power-law amplitude is increased by more than 76%. The enhanced heat transport in the rough cell cannot be explained by simple geometrical changes introduced by the rough surfaces, such as the effective height and contact area of the convection cell. The flow visualization reveals that the emission dynamics of the thermal plumes over the rough surface is changed completely. It is found that the interaction between the horizontal shear flow due to the large-scale circulation and the ordered rough surface creates a secondary

flow (eddies) in the groove region. This secondary flow together with the large-scale circulation enhance the detachment of the thermal boundary layer near the tip of the rough elements. Because the plume eruption over the rough surface is driven mainly by the large-scale flow rather than the buoyancy force, most thermal plumes in the rough cell lose their mushroom cap.

To quantitatively characterize the temperature fluctuations in the rough cell, we conducted a series of local temperature measurements over varying Rayleigh numbers and at various spatial positions near the rough surface. The near-wall temperature measurements reveal that the emission frequency of the thermal plumes is increased greatly near the tip of the rough elements. We believe that the extra thermal plumes detached from the rough elements are responsible for the enhanced heat transport in the rough cell. The local temperature measurements indicate that the thermal boundary layer follows the contour of the rough surface. The boundary layer thickness is found to be increased in the groove region but is reduced considerably near the tip when compared with that in the smooth cell. The small eddies trapped in the groove region produce a strong mixing effect, which suppresses the emission of the thermal plumes deep inside the groove and at the same time creates large temperature fluctuations outside the boundary layer. This non-uniform emission dynamics of the thermal plumes destroys the temperature homogeneity over the (cold) rough surface and produces a higher surface temperature at the tip of the rough elements. We believe that the lateral surface inhomogeneity is a general feature for turbulent heat transport over a rough surface, so long as the time scales associated with the boundary layer dynamics are shorter than the thermal diffusion time between the tip and groove over the solid plate. The striking effects of the surface roughness reported in this paper provide new insights into the roles played by the thermal plumes in determining the heat transport in turbulent convection. The discovery of the enhanced heat transport in the rough cell has important applications in engineering for more efficient heat transfer.

We thank H. J. Swinney, J. R. Herring, J. Werne and A. Belmonte for useful discussions. The assistance of M. Lucas and his team in fabricating the convection cells is gratefully acknowledged. This work was supported by the National Science Foundation under Grant No. DMR-9623612.

REFERENCES

Adrian, R. J., Ferreira, R. T. D. S. & Boberg, T. 1986 Turbulent thermal convection in wide horizontal fluid layers. *Exps. Fluids* **4**, 121–141.

Batchelor, G. K. 1967 *An Introduction to Fluid Dynamics*, p. 325. Cambridge University Press.

Belmonte, A., Tilgner, A. & Libchaber, A. 1993 Boundary layer length scales in thermal turbulence. *Phys. Rev. Lett.* **70**, 4067–4070.

Belmonte, A., Tilgner, A. & Libchaber, A. 1995*a* Temperature and velocity boundary layers in turbulent convection. *Phys. Rev.* E **50**, 269–279.

Belmonte, A., Tilgner, A. & Libchaber, A. 1995*b* Turbulence and internal waves in side-heated convection. *Phys. Rev.* E **51**, 5681–5687.

Castaing, B., Gunaratne, G., Heslot, F., Kadanoff, L., Libchaber, A., Thomae, S., Wu, X.-Z., Zaleski, S. & Zanetti, G. 1989 Scaling of hard turbulence in Rayleigh–Bénard convection. *J. Fluid Mech.* **204**, 1–30.

Chavanne, X., Chillá, F., Castaing, B., Hebral, B., Chabaud, B. & Chaussy, J. 1997 Observation of the ultimate regime in Rayleigh–Bénard convection. *Phys. Rev. Lett.* **79**, 3648–3651.

Chillá, F., Ciliberto, S., Innocenti, C. & Pampaloni, E. 1993 Boundary layer and scaling properties in turbulent thermal convection. *Il Nuovo Cimento* **15D**, 1229–1249.

Choi, H., Moin, P. & Kim, J. 1993 Direct numerical simulation of turbulent flow over riblets. *J. Fluid Mech.* **255**, 503–539.

Chu, Y. T. & Goldstein, R. J. 1973 Turbulent convection in a horizontal layer of water. *J. Fluid Mech.* **60**, 141–159.

Ciliberto, S., Cioni, S. & Laroche, C. 1996 Large-scale flow properties of turbulent thermal convection. *Phys. Rev.* E **54**, R5901–R5904.

Ciliberto, S. & Laroche, C. 1999 Random roughness of boundary increases the turbulent scaling exponent. *Phys. Rev. Lett.* **82**, 3998–4001.

Cioni, S., Ciliberto, S. & Sommeria, J. 1996 Experimental study of high-Rayleigh-number convection in mercury and water. *Dyn. Atmos. Oceans* **24**, 117–127.

Cioni, S., Ciliberto, S. & Sommeria, J. 1997 Strongly turbulent Rayleigh–Bénard convection in mercury: comparison with results at moderate Prandtl number. *J. Fluid Mech.* **335**, 111–140.

Dabiri, D. & Gharib, M. 1991 Digital particle image thermometry: the method and implementation. *Exps. Fluids* **11**, 77–86.

Deluca, E. E., Werne, J., Rosner, R. & Cattaneo, F. 1990 Numerical simulations of soft and hard turbulence: preliminary results for two-dimensional convection. *Phys. Rev. Lett.* **64**, 2370–2373.

Du, Y.-B. & Tong, P. 1998 Enhanced heat transport in turbulent convection over a rough surface. *Phys. Rev. Lett.* **81**, 987–990.

Du, Y.-B. & Tong, P. 2000 Temperature fluctuations in turbulent thermal convection under different boundary conditions. (To be submitted to *Phys. Rev.* E.)

Faber, T. E. 1995 *Fluid Dynamics for Physicists*, p. 252. Cambridge University Press.

Grossmann, S. & Lohse, D. 2000 Scaling in thermal convection: a unifying theory. *J. Fluid Mech.* **407**, 27–56.

Heslot, F., Castaing, B. & Libchaber, A. 1987 Transition to turbulence in helium gas. *Phys. Rev.* A **36**, 5870–5873.

Kerr, R. 1996 Rayleigh number scaling in numerical convection. *J. Fluid Mech.* **310**, 139–179.

Kraichnan, R. H. 1962 Turbulent thermal convection at arbitrary Prandtl number. *Phys. Fluids* **5**, 1374–1389.

Liu, Y.-M. & Ecke R. E. 1997 Heat transport scaling in turbulent Rayleigh–Bénard convection: effects of rotation and Prandtl number. *Phys. Rev. Lett.* **79**, 2257–2260.

Moin, P. & Bewley, T. 1994 Feedback control of turbulence. *Appl. Mech. Rev.* **47**, No. 6, part 2, S3–S13.

Moin, P. & Kim, J. 1997 Tackling turbulence with supercomputer. *Scientific American* January, 62–68.

Moses, E., Zocchi, G. & Libchaber, A. 1993 An experimental study of laminar plumes. *J. Fluid Mech.* **251**, 581–601.

Raupach, M. R., Antonia, R. A. & Rajagopalan, S. 1991 Rough-wall turbulent boundary layers. *Appl. Mech. Rev.* **44**, 1–25.

Riley, J. J., Gad-el-Hak, M. & Metcalfe, R. W. 1988 Compliant coatings. *Ann. Rev. Fluid Mech.* **20**, 393–420.

She, Z.-S. 1989 On the scaling laws of thermal turbulent convection. *Phys. Fluids* A **1**, 911–913.

Shen, Y., Tong, P. & Xia, K.-Q. 1996 Turbulent convection over rough surfaces. *Phys. Rev. Lett.* **76**, 908–911.

Shen, Y., Xia, K.-Q. & Tong, P. 1995 Measured local-velocity fluctuations in turbulent convection. *Phys. Rev. Lett.* **75**, 437–440.

Shraiman, B. I. & Siggia, E. D. 1990 Heat transport in high-Rayleigh-number convection. *Phys. Rev.* A **42**, 3650–3653.

Siggia, E. D. 1994 High Rayleigh number convection. *Ann. Rev. Fluid Mech.* **26**, 137–168.

Solomon, T. H. & Gollub, J. P. 1990 Sheared boundary layers in turbulent Rayleigh–Bénard convection. *Phys. Rev. Lett.* **64**, 2382–2385.

Solomon, T. H. & Gollub, J. P. 1991 Thermal boundary layers and heat flux in turbulent convection: the role of recirculating flows. *Phys. Rev.* A **43**, 6683.

Takeshita, T., Segawa, T., Glazier, J. G. & Sano, M. 1996 Thermal turbulence in mercury. *Phys. Rev. Lett.* **76**, 1465–1468.

Tanaka, H. & Miyata, H. 1980 Turbulent natural convection in a horizontal water layer heated from below. *Intl J. Heat Mass Transfer* **23**, 1273–1281.

Tennekes, H. & Lumley, J. L. 1972 *A First Course in Turbulence*. MIT Press.

Threlfall, D. C. 1975 Free convection in low temperature gaseous helium. *J. Fluid Mech.* **67**, 17–28.

Tong, P. & Shen, Y. 1992 Relative velocity fluctuations in turbulent Rayleigh–Bénard convection. *Phys. Rev. Lett.* **69**, 2066–2069.

Turner, J. S. 1962 The starting plume in neutral surroundings. *J. Fluid Mech.* **13**, 356–368.

Villermaux, E. 1998 Transfer at rough sheared interfaces. *Phys. Rev. Lett.* **81**, 4859–4862.

Walsh, M. J. 1990 Riblets. In *Viscous Drag Reduction in Boundary Layers* (ed. D. M. Bushnell & J. N. Hefner). Progress in Astro. and Aeronautics, vol. 123, pp. 203–261. AIAA.

Werne, J. 1993 Structure of hard-turbulence convection in two dimensions: numerical evidence. *Phys. Rev.* E **48**, 1020–1035.

Werne, J. 1994 Plume model for the boundary layer dynamics in hard turbulence. *Phys. Rev.* E **49**, 4072–4076.

Wu, X.-Z., Kadanoff, L., Libchaber, A. & Sano, M. 1990 Frequency power spectrum of temperature fluctuations in free convection. *Phys. Rev. Lett.* **64**, 2140–2143.

Xia, K.-Q. & Lui, Siu-Lung 1997 Turbulent thermal convection with an obstructed sidewall. *Phys. Rev. Lett.* **79**, 5006–5009.

Xin, Y.-B., Xia, K.-Q. & Tong, P. 1996 Measured velocity boundary layers in turbulent convection. *Phys. Rev. Lett.* **77**, 1266–1269.

Zocchi, G., Moses, E. & Libchaber, A. 1990 Coherent structures in turbulent convection, an experimental study. *Physica* A **166**, 387–407.